Current Optics and Photonics
Vol. 2, No. 2, April 2018, pp. 179-184

ISSN: 2508-7266(Print) / ISSN: 2508-7274(Online)
DOI: https://doi.org/10.3807/COPP.2018.2.2.179

Periodically Poled $BaTiO_3$: An Excellent Crystal for Terahertz Wave Generation by Cascaded Difference-frequency Generation

Zhongyang Li*, Bin Yuan, Silei Wang, Mengtao Wang, and Pibin Bing

College of Electric Power, North China University of Water Resources and Electric Power, Zhengzhou, Henan 450045, China

(Received November 25, 2017 : revised January 24, 2018 : accepted January 25, 2018)

Terahertz (THz) wave generation by periodically poled $BaTiO_3$ (PPBT) with a quasi-phase-matching (QPM) scheme based on cascaded difference-frequency generation (DFG) is theoretically analyzed. The cascaded DFG processes comprise cascaded Stokes and anti-Stokes processes. The calculated results indicate that the cascaded Stokes processes are stronger than the cascaded anti-Stokes processes. Compared to a noncascaded Stokes process, THz intensities from 20^{th}-order cascaded Stokes processes increase by a factor of 30. THz waves with a maximum intensity of 0.37 MW/mm^2 can be generated by 20^{th}-order cascaded DFG processes when the optical intensity is 10 MW/mm^2, corresponding to a quantum conversion efficiency of 1033%. The high quantum conversion efficiency of 1033% exceeds the Manley-Rowe limit, which indicates that PPBT is an excellent crystal for THz wave generation via cascaded DFG.

Keywords : Terahertz wave, Cascaded difference frequency generation, Periodically poled $BaTiO_3$
OCIS codes : (190.4410) Nonlinear optics, parametric processes; (140.3070) Infrared and far-infrared lasers

I. INTRODUCTION

Difference-frequency generation (DFG) has proved to be an efficient scheme to generate terahertz (THz) waves [1-4]. DFG offers the advantages of compactness, narrow linewidth, wide tuning range, high peak power, and room-temperature operation. However, the quantum conversion efficiency of DFG is relatively low. To improve the low quantum conversion efficiency and overcome the Manley-Rowe limit, cascaded DFG, in which more than one THz photon is generated from the depletion of a single pump photon, is a promising method. Theoretical descriptions and experimental demonstrations of enhancement of THz wave generation via cascaded DFG have been reported [5-9].

Nonlinear optical crystals, such as $ZnGeP_2$, GaSe, GaAs, GaP, and organic optical crystals, are characterized by large second-order nonlinear optical coefficients, which are employed to generate THz waves via DFG. THz waves are generated by DFG with collinear phase matching in birefringent crystals of $ZnGeP_2$ [10] and GaSe [11], with collinear phase matching in the organic crystal OH1 [12], and with noncollinear phasematching in zincblende-structure crystals of GaAs [13] and GaP [14], as well as with collinear phase matching in GaP [15]. Crystals with periodic variation of the $\chi^{(2)}$ nonlinear optical coefficient can solve the problem of wave-vector mismatch in DFG process, via quasi-phase-matching (QPM). THz wave generation by DFG in a QPM crystal with a nanosecond pulse was first demonstrated in periodically poled $LiNbO_3$ (PPLN) [16], and recently was demonstrated in periodically inverted GaP [17], periodically inverted GaAs [18] and periodically poled $KTiOPO_4$ (PPKTP) [19].

Similar to the above nonlinear optical crystals, $BaTiO_3$ is an attractive material for the nonlinear optical interaction between optical and THz waves, due to its wide transmission range (0.4-5 μm) [20], a relatively high second-order nonlinear optical coefficient (d_{15} = 13.7 pm/V at 1064 nm) [21], and a high optical damage threshold of 83 GW/cm^2 at 596 nm with a 1-ps pulse width [22]. At room temperature, the lattice vibrational modes of $BaTiO_3$ are split into three A_1

*Corresponding author: thzwave@163.com, ORCID 0000-0001-8350-5781
Color versions of one or more of the figures in this paper are available online.

and four E infrared-active and Raman-active transverse optical (TO) modes, and one B_1 Raman-active mode [23]. The four E TO modes in the tetragonal phase, with frequencies of 34 cm^{-1}, 180 cm^{-1}, 308 cm^{-1} and 498 cm^{-1}, are doubly degenerate, having their polarizations along the x and y axes [24]. The three A_1 TO modes in the tetragonal phase, with frequencies of 178 cm^{-1}, 260 cm^{-1} and 515 cm^{-1}, are polarized along the z axis [25]. The nonlinear susceptibility induced by TO modes can be employed to enhance the effective nonlinear optical coefficients involving both second-order and third-order nonlinear optical coefficients [26]. Periodically poled $BaTiO_3$ (PPBT) offers several advantages in THz wave generation by DFG. First, the coercive electric field required for domain reversal is 100 V/mm, which should allow fabrication of PPBT with wider apertures [27]. Second, the transmissivity at 4-5 μm is greater than 90% (for 1-cm crystal length), which is larger than in PPLN. Third, while the second-order nonlinear optical coefficient of PPBT is smaller than that of PPLN, the effective nonlinear optical coefficient of PPBT is larger.

In this manuscript, we theoretically investigate THz wave generation by PPBT with a QPM scheme based on cascaded DFG processes. We analyze both the cascaded Stokes processes and the cascaded anti-Stokes processes. The effective nonlinear optical coefficients of PPBT are calculated. According to coupled wave equations, we calculate THz intensities and quantum conversion efficiencies.

II. THEORETICAL MODEL

Figure 1 shows a schematic diagram of THz wave generation with PPBT by QPM cascaded DFG. The wave vectors of pump wave $\boldsymbol{K}_p$, first-order Stokes wave $\boldsymbol{K}_s$, and THz wave $\boldsymbol{K}_T$ are all parallel to the x axis. The electric field vectors of pump wave $\boldsymbol{E}_p$ and first-order Stokes wave $\boldsymbol{E}_s$ are perpendicular to the optical axis (z axis), whereas THz wave $\boldsymbol{E}_T$ is parallel to the optical axis (z axis). The THz wave is generated via interactions between the incident pump wave and first-order Stokes wave in the first-order Stokes process, which consumes the higher-frequency pump photon and amplifies the lower-frequency first-order Stokes photon. The amplified first-order Stokes wave also acts as a higher-frequency pump wave, which amplifies the THz wave and generates a new lower-frequency cascaded Stokes (ω_{cs}) wave in the second-order Stokes process. Simultaneously, anti-Stokes interactions will also occur and consume the THz photon and pump photon, resulting in a higher-frequency anti-Stokes wave (ω_{cp}). The cascaded Stokes and anti-Stokes processes can be continued to any high order, as long as the phase-matching conditions are satisfied. The intensity of the THz wave is determined by a trade-off between the Stokes processes and the anti-Stokes processes.

The coupled wave equations of the cascaded DFG can be derived from the common nonlinear optical three-wave interaction equations, shown as

$$\frac{dE_T}{dz} = -\frac{\alpha_T}{2}E_T + \kappa_T \sum_1^{+\infty} E_n E_{n+1} \cos\left(\Delta k_n z\right) \tag{1}$$

$$\frac{dE_n}{dz} = -\frac{\alpha_n}{2}E_n + \kappa_n E_{n-1} E_T \cos\left(\Delta k_{n-1} z\right) - \kappa_n E_{n+1} E_T \cos\left(\Delta k_n z\right) \tag{2}$$

$$\kappa_n = \frac{\omega_n d_{eff}}{c n_n} \tag{3}$$

$$\kappa_T = \frac{\omega_T d_{eff}}{c n_T} \tag{4}$$

$$\Delta k_n = k_n - k_{n+1} - k_T + 2\pi/\Lambda \tag{5a}$$

$$\Delta k_n = k_n - k_{n+1} + k_T - 2\pi/\Lambda \tag{5b}$$

$$\omega_T = \omega_n - \omega_{n-1} \tag{6}$$

$$I = \frac{1}{2} n c \varepsilon_0 |E|^2 \tag{7}$$

where ω_n and ω_T denote the frequency, E_n and E_T denote the electric field amplitude, α_n and α_T denote the absorption coefficient, κ_n and κ_T are the coupling coefficient, and n_n and n_T are the refractive index, with the subscripts n and T denoting the cascaded optical wave and THz wave respectively. Δk_n indicates the wave-vector mismatch in the cascaded forward DFG (Eq. (5a)) and cascaded backward DFG (Eq. (5b)), as shown in the inset of Fig. 1. d_{eff} is the effective nonlinear optical coefficient, c is the speed of light

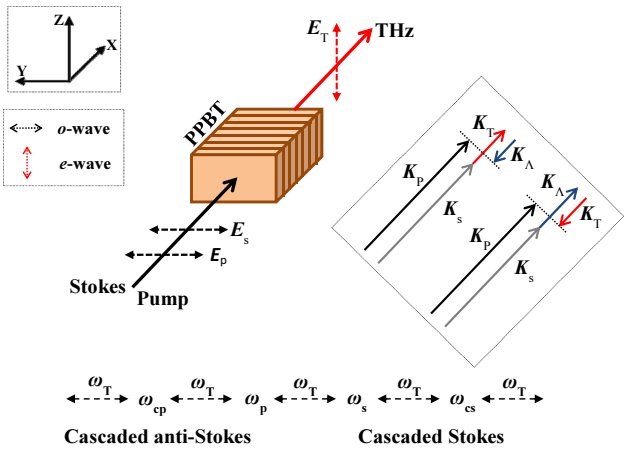

FIG. 1. Schematic diagram of the cascaded DFG generating a THz wave with PPBT. The wave vectors of pump, Stokes, and THz waves are all parallel to the x axis. The electric field vectors of pump ($\boldsymbol{E}_p$) and Stokes ($\boldsymbol{E}_s$) waves are perpendicular to the optical axis (z axis), and that of the THz wave ($\boldsymbol{E}_T$) is parallel to the optical axis (z axis). The pump wave, Stokes wave, and THz wave are o-wave, o-wave, and e-wave respectively.

in vacuum, ε_0 is the vacuum dielectric constant, Λ is the poling period of PPBT crystal, and I is the power density. The theoretical values of the refractive index are calculated using a wavelength-dependent Sellmeier equation for PPBT in the infrared [20] and THz [25] range, respectively.

For high-power THz wave generation by cascaded DFG, the magnitude of the nonlinear optical coefficient is important. We calculate the effective nonlinear optical coefficient d_{eff} and THz wave absorption coefficient α_T using the theoretical model proposed by Sussman [26],

$$d_{eff} = d_E + \sum_j \frac{S_j \omega_{0_j}^2 d_{Q_j}}{\omega_{0_j}^2 - \omega_T^2} \tag{8}$$

$$\alpha_T = 2\frac{\omega_T}{c}\mathrm{Im}(\varepsilon_\infty + \sum_j \frac{S_j \omega_{0_j}^2}{\omega_{0_j}^2 - \omega_T^2 - i\omega_T \Gamma_j})^{\frac{1}{2}} \tag{9}$$

where ω_{0_j}, S_j and Γ_j denote respectively the eigenfrequency, oscillator strength, and the bandwidth of the j^{th} A_1-symmetry phonon mode in the $BaTiO_3$ crystal. ε_∞ is the high-frequency dielectric constant. $d_E = 16\pi d_{15}$ and d_Q are nonlinear optical coefficients related to pure parametric (second-order) and Raman (third-order) scattering processes respectively. To take advantage of the largest nonlinear optical coefficient d_{15} of $BaTiO_3$, we consider that the pump wave, the first-order Stokes wave, and the THz wave are *o*-wave, *o*-wave, and *e*-wave respectively, as shown in the Fig. 1.

When the THz frequencies are far below the lowest TO mode of 178 cm^{-1}, Eq. (8) can be rewritten as

$$d_{eff} = d_E + \sum_j S_j d_{Q_j} \tag{10}$$

The relationship between d_E and d_Q is given by [26, 28, 29]

$$d_E + \sum_j S_j d_{Q_j} = \frac{1}{4} r_{51} n_n^4 \tag{11}$$

where r_{51} is the electro-optic coefficient of $BaTiO_3$, and r_{51} is 1640 pm/V at 546.1 nm for the unclamped $BaTiO_3$ [30].

III. CALCULATIONS

In simulating the cascaded DFG processes, the initial input pump wavelength and first-order Stokes wavelength are 546.1 nm and 547.1 nm, corresponding to ω_p and ω_s of 549.35 THz and 548.35 THz respectively. THz frequency ω_T is taken to be 1.0 THz. The wave-vector mismatch Δk_n and coherence length L_n in cascaded Stokes and anti-Stokes processes are shown in Fig. 2. Figure 2(a) shows forward cascaded DFG with Λ of 661.6 μm. In the shaded area, both wave-vector mismatches Δk_n in 4th-order cascaded Stokes and anti-Stokes processes are less than 3.14 cm^{-1} in forward cascaded DFG processes. Both wave-vector mismatches Δk_n in 20th-order cascaded Stokes and anti-Stokes processes are less than 15 cm^{-1}. According to the relation $L_n = \pi/\Delta k_n$, the wave-vector mismatches of 3.14 cm^{-1} and 15 cm^{-1} correspond to coherent lengths L_n of 1 cm and 0.21 cm respectively. Figure 2(b) shows backward cascaded DFG with Λ of 48.2 μm. In the shaded area, both wave-vector mismatches Δk_n in 4th-order cascaded Stokes and anti-Stokes processes are less than 3.14 cm^{-1} in backward cascaded DFG processes. Both wave-vector mismatches Δk_n in 20th-order cascaded Stokes and anti-Stokes processes are less than 15 cm^{-1}.

According to Eqs. (1)~(7), we calculate the intensities of the THz and optical waves in first-order backward Stokes process, assuming both the initial input pump intensity I_p and first-order Stokes intensity I_s are 10 MW/mm^2, as shown in Fig. 3. According to Eqs. (8)~(11), the effective nonlinear optical coefficient d_{eff} is 14,200 pm/V at a pump wavelength of 546.1 nm, and the absorption coefficient at 1.0 THz is 8.84 cm^{-1}. The d_{eff} of 14,200 pm/V exceeds the largest values of the nonlinear optical coefficient d_E by many orders of magnitude [31]. The nonlinear optical coefficient d_E is purely electronic in origin, since all frequencies are

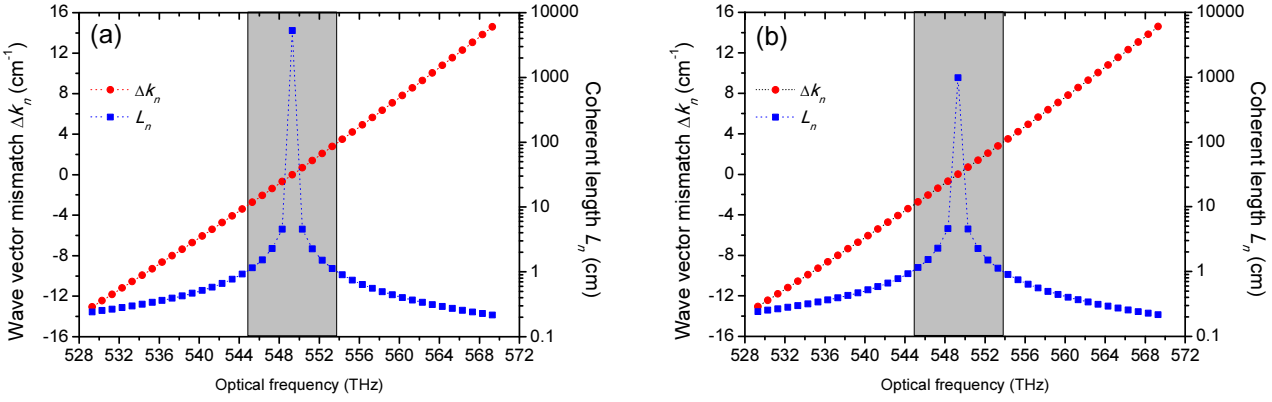

FIG. 2. Wave-vector mismatch Δk_n and coherence length L_n in cascaded DFG processes, assuming ω_p = 549.35 THz, ω_s = 548.35 THz, and ω_T = 1.0 THz: (a) forward cascaded DFG, Λ = 661.6 μm, (b) backward cascaded DFG, Λ = 48.2 μm.

above the lattice mode frequencies. The value of d_{eff} differs from that of d_E because d_Q lies below or close to the optical lattice mode frequencies, so that ionic as well as electronic anharmonicities induce large d_Q [32]. From Fig. 3 we find that the THz and optical wave intensities vary periodically with crystal length. The first maximum value of THz intensity is realized with a crystal length of 0.01 mm. The large effective nonlinear optical coefficient d_{eff} leads to fast energy conversion from optical wave to THz wave. The fast energy conversion within 0.01 mm allows THz generation in higher-order cascaded DFG processes, because the coherent length in 20th-order cascaded DFG processes is over 0.21 cm. As shown in Fig. 4, THz intensities in backward cascaded Stokes processes with cascaded orders of 1, 3, 7, 10, 15 and 20 are calculated. From the figure we find that THz intensities without cascaded processes are extremely low. THz intensities with cascaded orders of 3, 7, 10, 15 and 20 are enhanced. A THz intensity of 0.54 MW/mm^2 can be obtained by 20th-order cascaded Stokes processes. Compared to the noncascaded Stokes process, THz intensities from 20th-order cascaded Stokes processes increase by a factor of 30. In a noncascaded Stokes process, at best, a single THz photon is generated from each pump photon. The cascaded Stokes processes can enhance the THz output, simply by generating several THz photons from each pump photon.

Figure 5 shows the influence of the anti-Stokes processes on the intensities of THz waves. The THz intensities in backward cascaded Stokes processes are larger than those in backward cascaded Stokes and anti-Stokes processes. The maximum THz intensity in backward cascaded Stokes processes is 0.54 MW/mm^2, whereas the maximum THz intensity in backward cascaded Stokes and anti-Stokes processes is 0.37 MW/mm^2. To enhance THz intensity, the cascaded anti-Stokes processes must be suppressed.

Phase matching in cascaded DFG is important, since high-order optical waves interact to generate the THz wave. Figure 6 shows the THz intensities in 20th-order backward cascaded DFG processes, with and without wave-vector

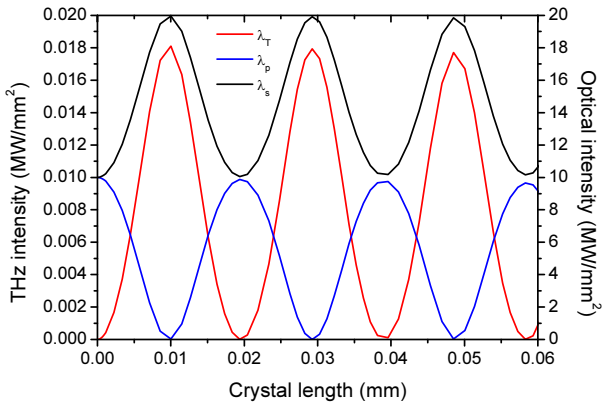

FIG. 3. THz and optical intensities in first-order backward Stokes process, assuming $I_p = I_s = 10$ MW/mm^2, $\Lambda = 48.2$ μm, $\omega_p = 549.35$ THz, $\omega_s = 548.35$ THz, and $\omega_T = 1.0$ THz.

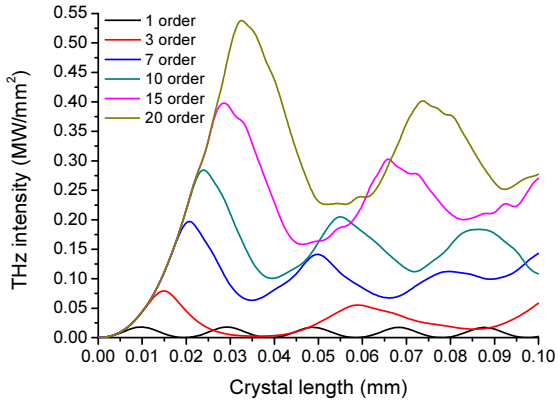

FIG. 4. THz intensities in backward cascaded Stokes processes with cascading orders of 1, 3, 7, 10, 15 and 20, assuming $I_p = I_s = 10$ MW/mm^2, $\Lambda = 48.2$ μm, $\omega_p = 549.35$ THz, $\omega_s = 548.35$ THz, and $\omega_T = 1.0$ THz.

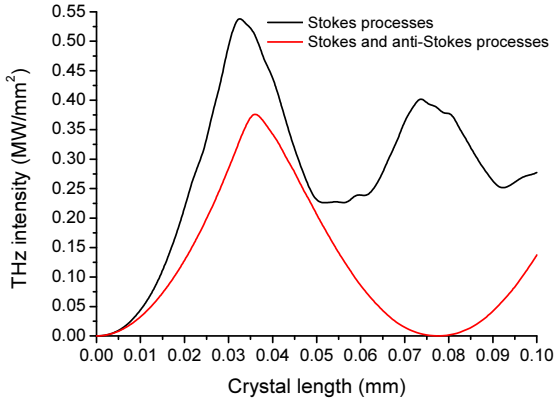

FIG. 5. THz intensities in 20th-order backward cascaded Stokes and anti-Stokes processes, assuming $I_p = I_s = 10$ MW/mm^2, $\Lambda = 48.2$ μm, $\omega_p = 549.35$ THz, $\omega_s = 548.35$ THz, and $\omega_T = 1.0$ THz.

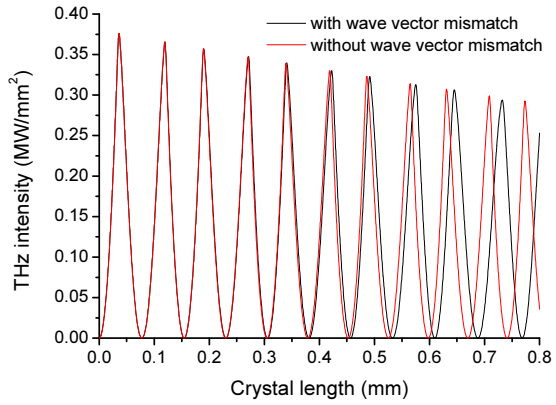

FIG. 6. THz intensities in 20th-order backward cascaded DFG processes, with and without wave-vector mismatch, assuming $I_p = I_s = 10$ MW/mm^2, $\Lambda = 48.2$ μm, $\omega_p = 549.35$ THz, $\omega_s = 548.35$ THz, and $\omega_T = 1.0$ THz.

mismatch. From the figure we find that THz intensities show no obvious difference between the cascaded DFG with and without wave-vector mismatch, whereas the position differences at the maximum THz intensities between the cascaded DFG with and without wave-vector mismatch gradually increase. The reason is that the large effective nonlinear optical coefficient d_{eff} leads to fast energy conversion from optical wave to THz wave within 0.05 mm. Wave-vector mismatch within 0.05 mm has little effect on cascaded DFG processes. With wave-vector mismatch, complete energy conversion from optical wave to THz wave requires a longer crystal length.

Since the cascaded Stokes processes generate THz photons and the cascaded anti-Stokes processes consume THz photons, THz intensity depends on the interaction between the cascaded Stokes and anti-Stokes processes. Figure 7 shows the maximum intensities of the optical waves during the 20th-order backward cascaded Stokes and anti-Stokes processes. From the figure we find that the

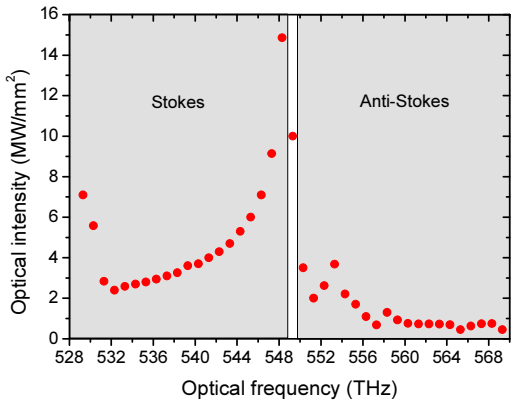

FIG. 7. The maximum intensities of the cascaded optical waves in 20th-order backward cascaded Stokes processes and anti-Stokes processes, assuming $I_p = I_s = 10$ MW/mm^2, $\Lambda = 48.2$ μm, $\omega_p = 549.35$ THz, $\omega_s = 548.35$ THz, and $\omega_T = 1.0$ THz.

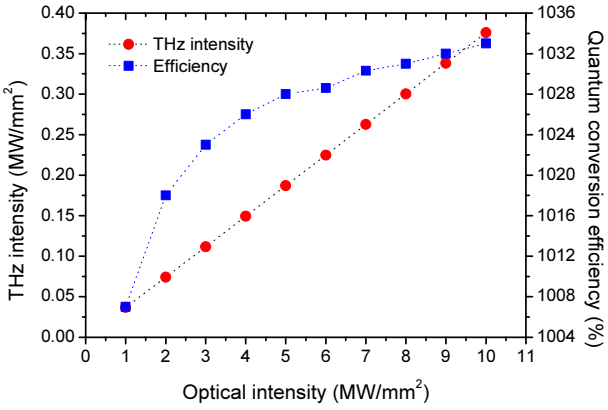

FIG. 8. THz intensities and quantum efficiencies versus optical intensities in 20th-order backward cascaded DFG processes, assuming $I_p = I_s$, $\Lambda = 48.2$ μm, $\omega_p = 549.35$ THz, $\omega_s = 548.35$ THz, and $\omega_T = 1.0$ THz.

intensities of optical waves in the Stokes processes are higher than those in the anti-Stokes processes, which indicates that the cascaded Stokes processes are stronger than the cascaded anti-Stokes processes.

Pump intensity is directly related to the quantum convertsion efficiency of a cascaded DFG processes. The maximum THz intensities and quantum conversion efficiencies in 20th-order backward cascaded DFG processes are calculated when the initial input pump wave and first-order Stokes wave intensities are varied from 1 to 10 MW/mm^2, as shown in Fig. 8. The figure demonstrates that the maximum THz intensities and quantum conversion efficiencies increase with the optical intensities. A THz wave with a maximum intensity of 0.37 MW/mm^2 can be generated with an optical intensity of 10 MW/mm^2, corresponding to a quantum conversion efficiency of 1033%, which exceeds the Manley-Rowe limit, indicating that PPBT is an excellent crystal for THz wave generation via cascaded DFG.

THz wave generation via cascaded DFG in PPBT has certain advantages over those in PPLN and PPKTP. First, the coercive electric field required for domain reversal is lower for PPBT than that for PPLN and PPKTP, which should allow fabrication of PPBT with wider apertures. Second, the effective nonlinear optical coefficients of PPBT are larger than those of PPLN and PPKTP, which indicates that PPBT can provide a higher gain in cascaded DFG.

IV. CONCLUSION

THz waves can be efficiently generated by PPBT via cascaded DFG processes. The calculated results indicate that cascaded Stokes processes are stronger than cascaded anti-Stokes processes. Compared to a noncascaded Stokes process, THz intensity from 20th-order cascaded Stokes processes increase 30-fold. Originating from the contributions of the second- and third-order nonlinear optical coefficients, the large effective nonlinear optical coefficients of PPBT enhance the generation of the THz wave. A THz wave with a maximum intensity of 0.37 MW/mm^2 can be generated in 20th-order cascaded DFG processes when the optical intensity is 10 MW/mm^2, corresponding to a quantum conversion efficiency of 1033%. The high generated THz intensity and quantum conversion efficiency indicate that PPBT is an excellent crystal for THz wave generation via cascaded DFG.

ACKNOWLEDGEMENT

This work was supported by the National Natural Science Foundation of China (Grant No. 61601183), Natural Science Foundation of Henan Province (Grant No. 162300410190), Program for Innovative Talents (in Science and Technology) in University of Henan Province (Grant No. 18HASTIT023), Young Backbone Teachers in University of Henan Province

(Grant No. 2014GGJS-065), and the Program for Innovative Research Team (in Science and Technology) in University of Henan Province (Grant No. 16IRTSTHN017).

REFERENCES

1. Y. J. Ding, "Progress in terahertz sources based on difference-frequency generation [Invited]," J. Opt. Soc. Am. B **31**, 2696-2711 (2014).
2. A. Majkić, M. Zgonik, A. Petelin, M. Jazbinšek, B. Ruiz, C. Medrano, and P. Günter, "Terahertz source at 9.4 THz based on a dual-wavelength infrared laser and quasi-phase matching in organic crystals OH1," Appl. Phys. Lett. **105**, 141115 (2014).
3. B. Dolasinski, P. E. Powers, J. W. Haus, and Adam Cooney, "Tunable narrow band difference frequency THz wave generation in DAST via dual seed PPLN OPG," Opt. Express **23**, 3669-3680 (2015).
4. K. Saito, T. Tanabe, and Y. Oyama, "Design of a GaP/Si composite waveguide for CW terahertz wave generation via difference frequency mixing," Appl. Opt. **53**, 3587-3592 (2014).
5. K. Ravi, M. Hemmer, G. Cirmi, F. Reichert, D. N. Schimpf, O. D. Mücke, and F. X. Kärtner, "Cascaded parametric amplification for highly efficient terahertz generation," Opt. lett. **41**, 3806-3809 (2016).
6. P. Liu, D. Xu, H. Yu, H. Zhang, Z. Li, K. Zhong, Y. Wang, and J. Yao, "Coupled-mode theory for Cherenkov-type guided-wave terahertz generation via cascaded difference frequency generation," J. Lightw. Technol. **31**, 2508-2514 (2013).
7. A. J. Lee and H. M. Pask, "Cascaded stimulated polariton scattering in a Mg:$LiNbO_3$ terahertz laser," Opt. Express **23**, 8687-8698 (2015).
8. K. Saito, T. Tanabe, and Y. Oyama, "Cascaded terahertz-wave generation efficiency in excess of the Manley-Rowe limit using a cavity phase-matched optical parametric oscillator," J. Opt. Soc. Am. B **32**, 617-621 (2015).
9. G. Cirmi, M. Hemmer, K. Ravi, F. Reichert, L. E. Zapata, A. L. Calendron, H. Cankaya, F. Ahr, O. D. Mücke, and F. X. Kärtner, "Cascaded second-order processes for the efficient generation of narrowband terahertz radiation," J. Phys. B: At., Mol. Opt. Phys. **50**, 044002 (2017).
10. W. Shi and Y. J. Ding, "Continuously tunable and coherent terahertz radiation by means of phase-matched difference-frequency generation in zinc germanium phosphide," Appl. Phys. Lett. **83**, 848-850 (2003).
11. W. Shi and Y. J. Ding, "Generation of backward terahertz waves in GaSe crystals," Opt. Lett. **30**, 1861-1863 (2005).
12. H. Uchida, S. R. Tripathi, K. Suizu, T. Shibuya, T. Osumi, and K. Kawase, "Widely tunable broadband terahertz radiation generation using a configurationally locked polyene 2-[3-(4-hydroxystyryl)-5, 5-dimethylcyclohex-2-enylidene] malononitrile crystal via difference frequency generation," Appl. Phys. B **111**, 489-493 (2013).
13. K. L. Vodopyanov, "Optical THz-wave generation with periodically-inverted GaAs," Laser Photon. Rev. **2**, 11-15 (2008).
14. T. Tanabe, K. Suto, J. Nishizawa, K. Saito, and T. Kimura, "Tunable THz wave generation in the 3- to 7-THz region from GaP," Appl. Phys. Lett. **83**, 237-239 (2003).
15. T. Taniuchi and H. Nakanishi, "Continuously tunable terahertz-wave generation in GaP crystal by collinear difference frequency mixing," Electron. Lett. **40**, 327-328 (2004).
16. Y. Sasaki, A. Yuri, K. Kawase, and H. Ito, "Terahertz-wave surface-emitted difference frequency generation in slant-stripe-type periodically poled $LiNbO_3$ crystal," Appl. Phys. Lett. **81**, 3323-3325 (2002).
17. Y. Jiang, Y. J. Ding, and I. B. Zotova, "Power scaling of widely-tunable monochromatic terahertz radiation by stacking high-resistivity GaP plates," Appl. Phys. Lett. **96**, 031101 (2010).
18. Y. Jiang, Y. J. Ding, and I. B. Zotova, "Power scaling of coherent terahertz pulses by stacking GaAs wafers," Appl. Phys. Lett. **93**, 241102 (2008).
19. H. Jang, A. Viotti, G. Strömqvist, A. Zukauskas, C. Canalias, and V. Pasiskevicius, "Counter-propagating parametric interaction with phonon-polaritons in periodically poled $KTiOPO_4$," Opt. Express **25**, 2677-2686 (2017).
20. D. E. Zelmon, D. L. Small, and P. Schunemann, "Refractive index measurements of barium titanate from .4 to 5.0 microns and implications for periodically poled frequency conversion devices," MRS Online Proc. Libr. Arch. **484**, 537-541 (1997).
21. D. N. Nikogosyan, *Nonlinear optical crystals: a complete survey* (Springer Science & Business Media, 2006).
22. T. F. Boggess, J. O. White, and G. C. Valley, "Two-photon absorption and anisotropic transient energy transfer in $BaTiO_3$ with 1-psec excitation," J. Opt. Soc. Am. B **7**, 2255-2258 (1990).
23. A. Pinczuk, W. Taylor, E. Burstein, and I. Lefkowitz, "The Raman spectrum of $BaTiO_3$," Solid State Commun. **5**, 429-433 (1967).
24. A. Scalabrin, A. S. Chaves, D. S. Shim, and S. P. S. Porto, "Temperature dependence of the A_1 and E optical phonons in $BaTiO_3$," Phys. Status Solidi B **79**, 731-742 (1977).
25. J. A. Sanjurjo, R. S. Katiyar, and S. P. S. Porto, "Temperature dependence of dipolar modes in ferroeiectric $BaTiO_3$ by infrared studies," Phys. Rev. B **22**, 2396-2403 (1980).
26. S. S. Sussman, "Tunable light scattering from transverse optical modes in lithium niobate," Stanford University, Stanford, California, Microwave Laboratory Report No. **1851** (1970).
27. S. D. Setzler, P. G. Schunemann, T. M. Pollak, and L. A. Pomeranz, "Periodically poled Barium Titanate as a new nonlinear optical material," Adv. Solid-State Lasers, Trends Opt. Photonics Ser. **MD1** (1999).
28. A. Yariv, *Quantum Electronics*, 3rd ed. (Wiley, 1988), Chapter 16.
29. W. D. Johnston and I. P. Kaminow, "Contributions to optical nonlinearity in GaAs as determined from Raman scattering efficiencies," Phys. Rev. **188**, 1209-1211 (1969).
30. A. R. Johnston and J. M. Weingart, "Determination of the low-frequency linear electro-optic effect in tetragonal $BaTiO_3$," J. Opt. Soc. Am. **55**, 828-834 (1965).
31. I. Shoji, T. Kondo, and R. Ito, "Second-order nonlinear susceptibilities of various dielectric and semiconductor materials," Opt. Quantum Electron. **34**, 797-833 (2002).
32. G. D. Boyd, T. J. Bridges, M. A. Pollack, and E. H. Turner, "Microwave nonlinear susceptibilities due to electronic and ionic anharmonicities in acentric crystals," Phys. Rev. Lett. **26**, 387-390 (1971).